Journal of Zhejiang University-SCIENCE A (Applied Physics & Engineering)
ISSN 1673-565X (Print); ISSN 1862-1775 (Online)
www.jzus.zju.edu.cn; www.springerlink.com
E-mail: jzus@zju.edu.cn

Novel integration methodology for an inward turning waverider forebody/inlet*

Wen-hao ZHANG, Jun LIU†‡, Feng DING, Wei HUANG

Science and Technology on Scramjet Laboratory, National University of Defense Technology, Changsha 410073, China

†E-mail: liujun_nudt@163.com

Received July 12, 2019; Revision accepted Sept. 26, 2019; Crosschecked Nov. 13, 2019

Abstract: In this study, an inward turning waverider forebody/inlet axisymmetric reference flow model with a conical leading-edge shock wave was designed based on the method of characteristics. The design eliminates the lip shock wave at the shoulder point. Based on the reference flow model, a novel integrated design method for an inward turning waverider forebody/inlet is proposed. The streamline tracing method and related technologies were used to generate the integrated configuration in the reference flow model. During the design process, the inward turning inlet was divided into an upper and a lower surface. After the formation of these surfaces, the front external surface and the lip external surface were simultaneously generated. Finally, an integrated configuration was formed with these four generated surfaces and a base plane. An analysis of the formed configuration was carried out using numerical simulation software, which verified the correctness and feasibility of the method. The conclusions drawn from the research indicate that the integrated design method is feasible and effective.

Key words: Hypersonic; Basic flow mode; Streamline tracing; Inward turning inlet
https://doi.org/10.1631/jzus.A1900334 **CLC number:** V22

1 Introduction

An integrated design of the inlet and the airframe is a very important factor for hypersonic flight to be realized (Barkmeyer et al., 2005; Tian et al., 2013; Li et al., 2014; Zuo et al., 2015, 2016; Wang et al., 2016; Wang WX et al., 2017). Well-designed integration of the airframe and inlet system could meet the comprehensive requirements of designers for aerodynamic and propulsion performance of hypersonic vehicles (Wang JF et al., 2017b; Liao et al , 2018).

From a design perspective, there are differences between these two requirements: the main requirements for the airframe are a high effective volume, excellent aerothermal performance of the leading-edge, and a high lift-drag ratio performance. The requirements for the inlet are the provision of several effective air sources for the combustor, along with minimum air flow energy loss (Heiser and Pratt, 1994).

In recent years, many long-range hypersonic vehicles have adopted a 3D inward turning inlet. Regardless of the intake mode, the inlet and airframe are highly integrated. The leading-edge affects both the performance of the intake ports and the aerodynamic characteristics of the aircraft (Zhou et al., 2018). A highly integrated airframe and 3D inward turning inlet is a goal actively pursued by researchers throughout the world (Walker and Rodgers, 2005; Walker et al., 2008; Ding et al., 2015, 2018; Wang JF et al., 2017a).

In this study, to exploit the inward turning inlet's high total pressure recovery coefficient and high compression rate characteristics, the inlet compression surface was considered to act directly as the

‡ Corresponding author
* Project supported by the National Natural Science Foundation of China (No. 11702322), and the Hunan Provincial Natural Science Foundation of China (No. 2018JJ3589)
ORCID: Wen-hao ZHANG, https://orcid.org/0000-0002-3514-3007

pre-compression surface of the aircraft's forebody. Several researchers have studied integrated configurations (Li et al., 2018; Qiao et al., 2018; Yang et al., 2019). Qiao et al. (2018) proposed an integration design method based on the shape of the forebody shock wave for the integrated design of a waverider forebody/inward turning inlet. The method achieves better matching between the shape of the capture section and inlet entrance line and the forebody shock wave. Ferguson et al. (2015) simulated the hypersonic flow field inside and around a generic hypersonic vehicle in detail, and analysed its on- and off-design performance. High-speed air is compressed by two shock waves (a leading-edge shock and a reflected shock) when entering the inlet under the selected flight condition. Kothari et al. (1996) proposed a hypersonic vehicle design code that creates and analyses various single-stage-to-orbit aircraft based on axisymmetric flow fields. These aircraft adopt an inverse design method and incorporate the concept of a radial deviation parameter into the calculation of the generated flow field. Wang et al. (2015) described a design method for the preliminary integration of a hypersonic vehicle fuselage structure and propulsion flow. The method is based mainly on integration of the variable cross-section inward turning inlet and the fuselage.

2 Design principles of an integrated inward turning waverider forebody/inlet

For the method presented in this paper, the inlet is divided into an upper surface and a lower surface (Fig. 1), which are formed in the reference flow model based on the streamline tracing technique. In addition, the integrated inward turning waverider forebody/inlet (ITWF) is formed with the inlet and three surfaces—the front external surface, the lip external surface, and the base surface. For simplicity, the front external surface is a free-stream surface. The design method for the lip external surface is discussed in Section 3.

Fig. 2 illustrates the inward turning waverider forebody/inlet axisymmetric reference flow model (IARFM), which consists of two shock waves and two walls. The centre body *DEF* and the axisymmetric generating body *ABCG* constitute the walls of the model. The wave structure of the model comprises two shock waves—the leading-edge shock wave *AD* and the lip shock wave *DC*. The region *ABCGFED* is established as the flow area of the reference flow model, to form the inward turning inlet. M_∞ is the Mach number of freestream; p_∞ is the pressure of freestream; T_∞ is the temperature of freestream.

The design principle of the proposed method is shown in Fig. 3. Under the design conditions, the leading-edge shock wave is produced when the axisymmetric generating body is determined, and the lip of the inlet is attached to the axisymmetric shock, thereby forcing higher pressure air below the lower surface. This means the higher pressure air does not spill over the upper surface, thereby allowing full flow capture to be achieved.

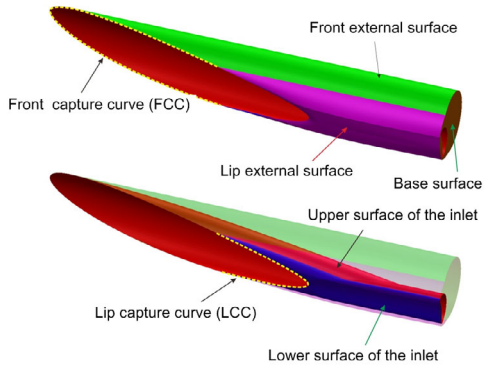

Fig. 1 Constituent parts of the integrated inward turning waverider forebody/inlet

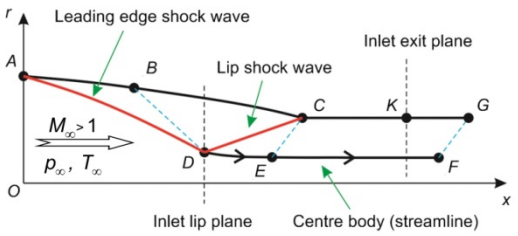

Fig. 2 Structure of the inward turning waverider forebody/inlet axisymmetric reference flow model

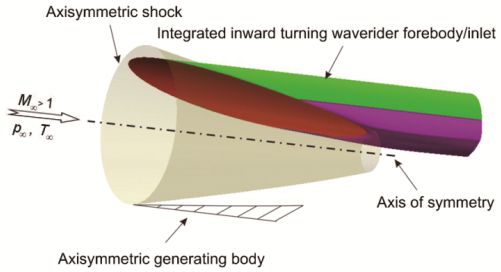

Fig. 3 Design principle of the integrated inward turning waverider forebody/inlet

3 Design methodology of the reference flow model

A novel integrated axisymmetric reference flow model is used herein from which the ITWF can be generated, based on the method of characteristics (MOC) (Zucrow and Hoffman, 1977) and the streamline tracing technique (Billig and Kothari, 2000). Adopting the design method from (Ding et al., 2015), the axisymmetric reference flow model of external compression is remodelled into the IARFM (Figs. 4–9), which is composed of the following four parts: (1) the dependent region of leading-edge shock wave *A*–*B*–*D*; (2) the isentropic principal compression region *B*–*C*–*D*; (3) the dependent region of lip shock wave *C*–*D*–*E*; (4) the stability region *C*–*E*–*F*–*G*.

The design process includes providing the wall position, and calculating of the iteration of the shock position and the flow field before and after the shock wave. The specific design steps are as follows.

First, as shown in Fig. 4, when the axisymmetric generating body ABC_2 is given, the leading-edge shock wave AR is generated, and the body is composed of a quadratic curve AB and a cubic curve BC_2. Given the tilt angle φ_A and the coordinates at point $A(x_A, r_A)$, the tilt angle φ_B and the x-coordinates of point $B(x_B)$, and the tilt angle φ_C and the coordinates of point $C(x_{C2}, r_{C2})$, the axisymmetric generating body ABC_2 is uniquely determined. Point R is an imaginary point of the leading-edge shock wave near the symmetric axis.

Second, as shown in Fig. 5, the right-running Mach line BD starting from point B intersects point D with the leading-edge shock wave AR. The inlet lip plane is defined as a cross-section passing through point D, and the position of point D needs to be calculated iteratively.

Third, as shown in Fig. 6, the left-running Mach line DC_1 passes through point D and intersects with the axisymmetric generating body ABC_2 at point C_1. The region is surrounded by the right-running Mach line BD, left-running Mach line DC_1, and axisymmetric generating body BC_1.

Fourth, as shown in Fig. 7, taking point D as the starting point of the lip shock wave, the flow angle of each point behind DC is given by

$$\theta_x = \theta(x), \quad x \in [x_D, x_C], \tag{1}$$

where $\theta(x)$ is the distribution of the flow angle θ behind DC, and is a function of x. The predictor-corrector iteration method is used to solve the position of the lip shock wave until the lip shock wave intersects the axisymmetric generating body BC_1 at shoulder point C. Next, the distribution of the flow parameters after the lip shock wave is solved by oblique shock wave theory. The region is surrounded by the right-running Mach line BD, lip shock wave DC, and axisymmetric generating body BC.

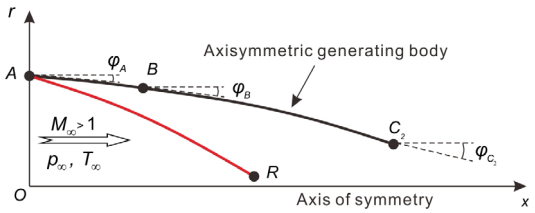

Fig. 4 Method for determining the position of the leading-edge shock wave *AR*

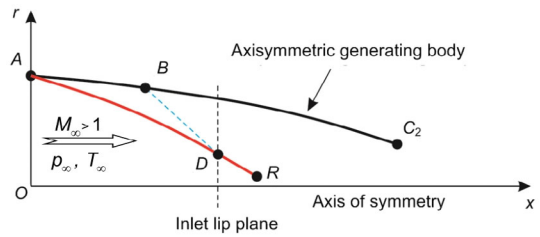

Fig. 5 Method to solve the region *A*-*B*-*D*

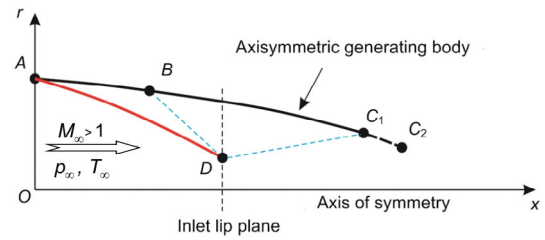

Fig. 6 Method to solve the region *B*-*D*-C_1

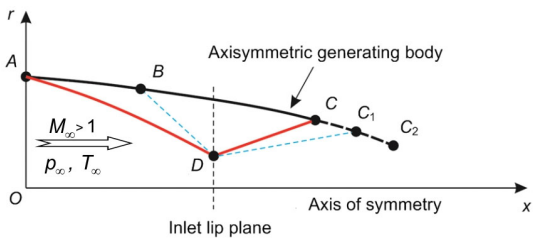

Fig. 7 Method to determine the position of the lip shock wave *DC*

Fifth, Fig. 8 illustrates the way to solve the streamline *DE*, which is represented by the solid arrow line. The dotted line *CE* is the left-running Mach line. The region *C*–*D*–*E* can be solved when the lip shock wave *DC* is determined and the properties of flow behind *DC* are solved, based on the MOC.

Finally, on the right side of shoulder point *C* in Fig. 9, the tilt angle $\varphi(x)$ of each point on body *CG* is expressed as φ_x:

$$\varphi_x = \varphi(x), \quad x \in [x_C, x_G]. \tag{2}$$

Similarly, the Mach number $M(x)$ of each point on body *CG* is expressed as M_x:

$$M_x = M(x), \quad x \in [x_C, x_G]. \tag{3}$$

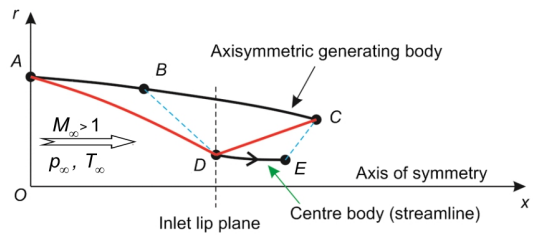

Fig. 8 Method to determine the position of the centre body *DE*

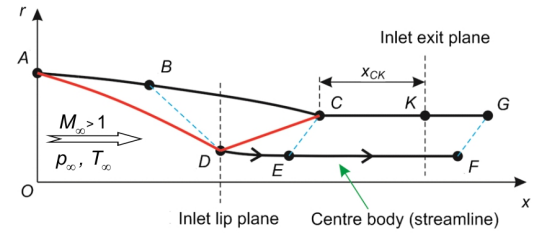

Fig. 9 Method to determine the position of body *CG*, centre body *EF*, and the inlet exit plane

Next, given the distance between the shoulder points *C* and *F* along the *x*-axis direction, x_{CF}, based on the MOC, the region *C*–*G*–*F*–*E* can be solved. The left-running Mach line *FG* intersects body *CG* at point *G*, and intersects the streamline *EF* at point *F*. Note that the tilt angle of the body *CG* at the shoulder point *C* must coincide with the directional angle of the local airflow to prevent the lip shock wave reflecting at the shoulder point and to produce the effect of wave elimination.

The *x*-axis distance between shoulder points *C* and *K* is x_{CK}, and the inlet exit plane is defined as the cross-section passing through point *K*. Based on the MOC, the four parts can be solved. In summary, with the design of the axisymmetric reference flow model, the field is obtained.

4 Geometric model and numerical method

In this part, a practical case is solved based on the presented integration method. The size characteristics of the corresponding generated model are shown in Fig. 10.

The parameters for the reference flow model are listed in Table 1. In this practical case, the curve *AB* is a quadratic curve and BC_2 is a cubic curve. Given the tilt angles φ_A, φ_B, φ_C, the point coordinates $A(x_A, r_A)$ and $C(x_{C2}, r_{C2})$, and the *x*-coordinate at point $B(x_B)$, the axisymmetric generating body ABC_2 can be determined. Note that the condition $M(x)=M_C$ means that the Mach number of each point on the body *CG* is equivalent to the Mach number at point *C*.

Table 1 Specific parameters for the reference flow model

M_∞	p_∞ (Pa)	T_∞ (K)	x_A (m)	x_B (m)	x_{C2} (m)	φ_A (°)
6.0	2511.18	221.649	0.1	1.28	11.2	2.5
φ_B (°)	φ_{C2} (°)	$\theta(x)$ (°)	$\varphi(x)$ (°)	$M(x)$	x_{CF} (m)	
5.5	10	0.0	0.0	M_C	1.0	

For the integrated configuration, the front capture curve (FCC) and lip capture curve (LCC) are expressed by the projection of the front capture curve (PFCC) and the projection of the lip capture curve (PLCC) on the base plane (Fig. 11). The projection line of the circular entrance is divided into two sections, PFCC and PLCC, by the two tangents, O_1M and O_1N. When the two sections are dispersed into several points, front capture curve points (FCCPs) and lip capture curve points (LCCPs) are generated by the intersection of the free streamline with the leading-edge shock wave at each discrete point. Each FCCP is connected to form an FCC curve, and each LCCP is connected to form an LCC curve.

In the reference flow model, the forebody streamline (FS) can be generated using streamline tracking from the FCCP to the inlet exit plane. Point 2

(Fig. 12) is an example of an FCCP. The FS goes through point 2 until exit-point 3; all the FSs form the upper surface of the inward turning inlet. The lip streamline (LS) can also be obtained from the LCCP using streamline tracking through point 5 until exit-point 6; all the LSs form the lower surface of the inward turning inlet. Therefore, the inward turning inlet consists of the upper and lower surfaces combined.

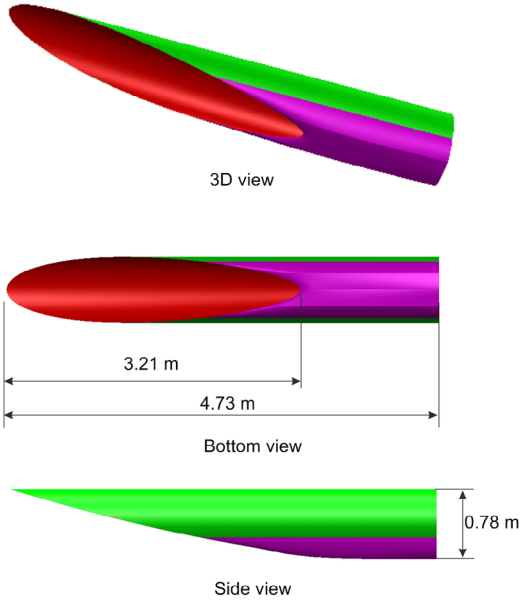

Fig. 10 Geometric model of a practical case

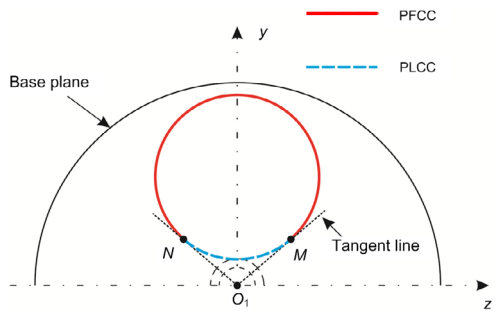

Fig. 11 Sketch map of the projection line on the base plane

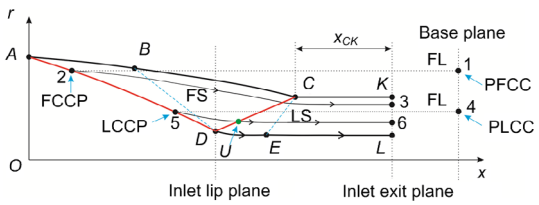

Fig. 12 Design of the forebody streamline (FS) and lip streamline (LS)

Note that for streamlines other than LCCPs, except at point D, the lip shock wave is generated at point U, which is the reflection point of the shock wave on the lower surface of the inward turning inlet, and also the intersection point of the LS and the lip shock wave.

Point 2 (Fig. 13) is an example in the plane that is parallel to the plane of symmetry; freestream line (FL) is generated from point 2 to exit-point 7. All the FLs form the front external surface. Furthermore, taking point 5 as an example, the lip external surface profile 5–8 is designed in the same plane. It is determined by the thickness Δd between LS and the lip external surface profile, expressed as

$$\Delta d = \Delta d(x),\ x \in [x_5, x_6]. \tag{4}$$

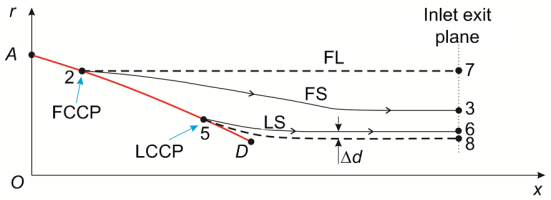

Fig. 13 Design of the profiles of the front external surface and lip external surface

ANSYS Fluent (Ansys Inc., 2010) software is used to simulate the inviscid flow field using the Euler equation. As in previous numerical simulation work of integrated configurations, in this model, a density-based (coupled) implicit solver is used to solve the Euler equation. The advection upstream splitting method (AUSM) is applied to the second-order spatially accurate upwind scheme of the flux vector, and the gradient is calculated based on the least-squares cell-based method. The Courant–Friedrichs–Lewy (CFL) number is set at 0.2. The airflow is set as the ideal gas. As mentioned above, convergence can be achieved after 8456 steps of iteration.

Fig. 14 illustrates the setting of boundary conditions and the unstructured grid in numerical computation. Specifically, for this case, inlet 1 is defined as the pressure far field boundary condition. Moreover, outlet 1 and outlet 2 are defined as the pressure outlet boundary condition. Owing to the symmetry of the geometric configuration, it is sufficient to solve half of the flow field, which can reduce computational

complexity. Finally, the number of unstructured grid cells of the half-model is kept at 2606344. The specified flight conditions for this case are listed in Table 2.

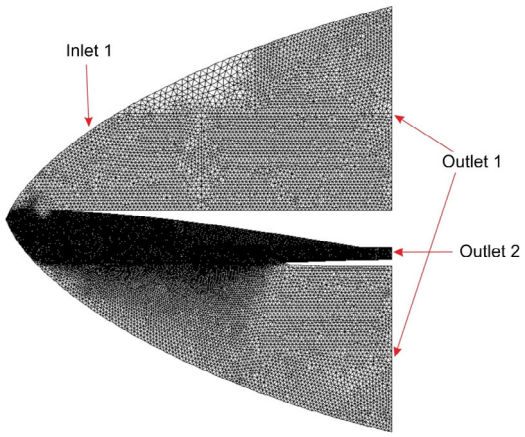

Fig. 14 Setting of boundary conditions and the unstructured grid in numerical computation

Table 2 Specified flight conditions

Parameter	Value
Angle of attack (°)	0
Flight Mach number	6.0
Cruising height (km)	25
Pressure of freestream, p_∞ (Pa)	2511.18
Temperature of freestream, T_∞ (K)	221.649

5 Numerical simulation and discussion

5.1 Verification of the IARFM

The Mach number contour and the inviscid non-dimensional pressure contour of the field of the reference flow model obtained by the MOC are illustrated in Figs. 15 and 16, respectively. Moreover, Figs. 17 and 18 illustrate the Mach number contour and the inviscid non-dimensional pressure contour of the field of the integrated configuration at the plane of symmetry, respectively. The structure of the flow field (Figs. 15 and 16) was obtained from the Euler code. The structures shown in Figs. 17 and 18 were obtained by the MOC. Clearly, there is no significant difference between the two structures.

The numerical simulation results shown above validate the correctness of the design methodology for the basic flow mode. The performance parameters of the reference flow model on the design point (inviscid condition) are presented in Table 3. Note that M_{exit} represents the Mach number, and p_{exit} represents the pressure, and p_{exit}/p_∞ and P_{exit}/P_0 represent the pressure rise ratio and total pressure recovery, respectively. P represents the total pressure and p represents the static pressure. All parameters were calculated by means of the area-weighted average method at the exit plane.

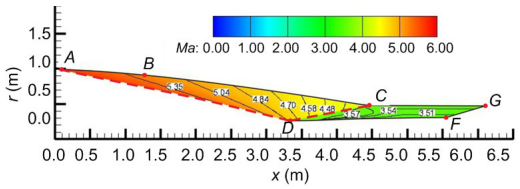

Fig. 15 Mach number contour of the reference flow model obtained by the MOC

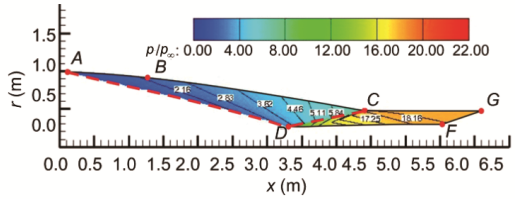

Fig. 16 Non-dimensional pressure contour of the reference flow model obtained by the MOC

5.2 Verification of the ITWF

The Mach number contour of the field of the integrated configuration at the plane of symmetry is shown in Fig. 17. The inviscid non-dimensional pressure contour of on-design at the plane of symmetry and the four chosen cross-sections of the integrated configuration field are shown in Figs. 18 and 19, respectively. The white dotted line in Fig. 17 and the red dotted line in Fig. 18 represent the theoretical design position of the leading-edge shock wave A_1D_1 and lip shock wave D_1C_1 at the symmetry plane. It is clear from Figs. 15 and 18 that the numerical simulation results of the shape and location of the shock wave are in accordance with those obtained using the MOC. As expected in the design, the lip shock wave is eliminated at the shoulder point C_1.

At each cross-section in Fig. 19, the red dotted line shows the theoretical design position of the leading-edge shock wave at each cross-section. The

higher pressure air is confined between the shock wave and the lower surface, which essentially achieves full flow capture. This indicates that the forebody can sit on the leading-edge shock wave on the design point, which validates the concept proposed herein. Furthermore, the total pressure recovery coefficient under inviscid conditions can reach the value of 0.87, which is the area-weighted average (Fig. 20). This also demonstrates the characteristics of the high total pressure recovery coefficient of the inward turning inlet.

Table 3 Inviscid performance of the inward turning waverider forebody/inlet axisymmetric reference flow mode (IARFM) and integrated inward turning waverider forebody/inlet (ITWF)

Model	M_{exit}	p_{exit}/p_∞	P_{exit}/P_0
IARFM	3.53	18.2	0.88
ITWF	3.52	18.8	0.87

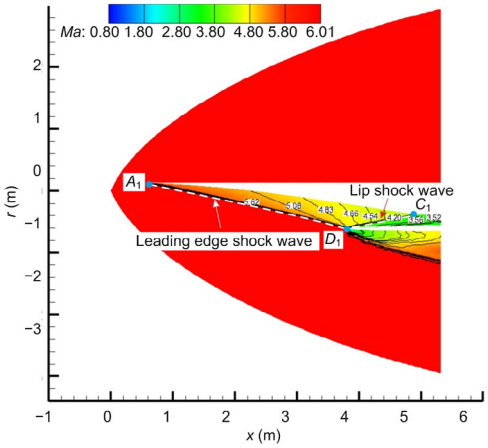

Fig. 17 Mach number contour in the symmetry plane of the case

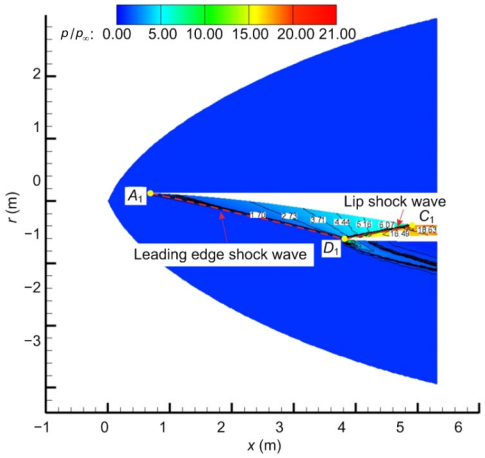

Fig. 18 Non-dimensional pressure contour in the symmetry plane of the case

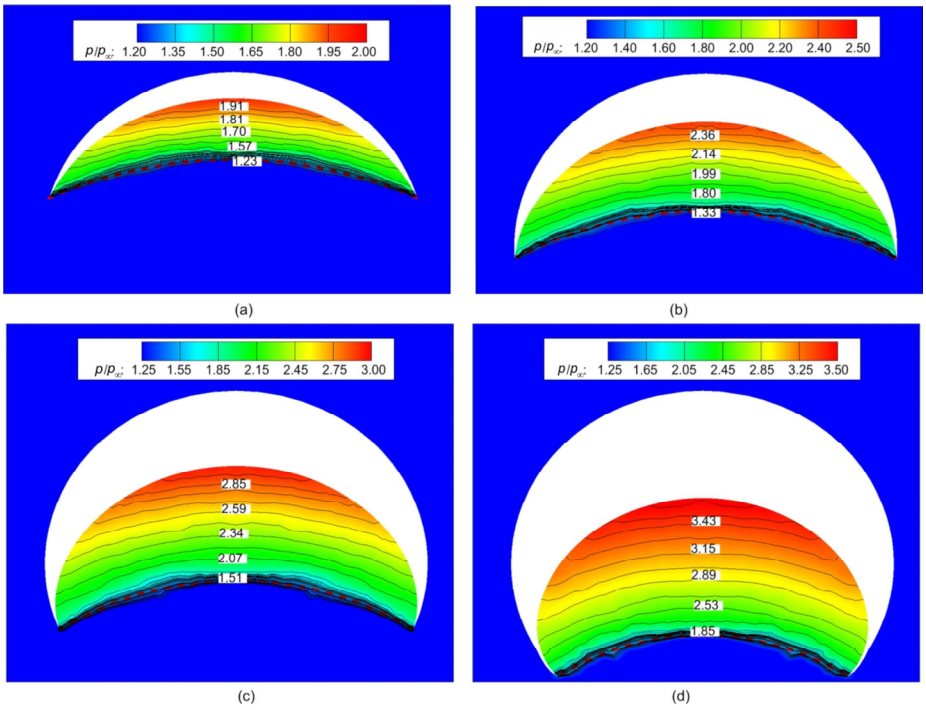

Fig. 19 Inviscid non-dimensional pressure contour at each cross-section of the case
(a) x=1.5 m; (b) x=2.0 m; (c) x=2.5 m; (d) x=3.0 m

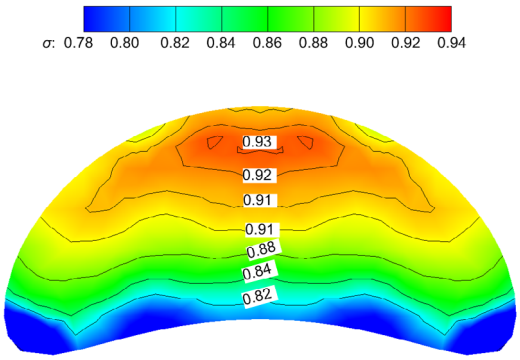

Fig. 20 Total pressure recovery coefficient in inlet exit plane

6 Conclusions

In this study, an integrated design method of an inward turning waverider forebody/inlet axisymmetric reference flow model was developed in which an integrated configuration was created. The research work included development of the design method, numerical simulation of the integrated configuration and verification of the method. Based on these studies, we can draw the following conclusions:

1. The axisymmetric reference flow model was designed based on the MOC. In this model, the inward turning inlet and the external surface were designed and generated simultaneously. During the design process, we proposed the concept of dividing the inlet capture curve into FCC and LCC, which we consider to be of physical significance.

2. The design method of the integrated configuration conforms to aerodynamic principles. In this paper, the accuracy and validity of the design method were verified by comparing the results of inviscid numerical simulation with theoretical design values. As shown in each cross-section of the ITWF, the higher pressure air is confined between the shock wave and the lower surface, which essentially achieves full flow capture. This indicates that the forebody of the integrated configuration can sit on the leading-edge shock wave on the design point (inviscid condition).

3. At the plane of symmetry of the integrated configuration, the numerical simulation results for the shape and location of the shock wave were in accordance with the axisymmetric reference flow model. The results presented above validate the correctness and feasibility of the design methodology for the integrated configuration under the inviscid condition. The numerical results verify that the integrated configuration has high flow capture efficiency and the designed inlet has a high total pressure recovery coefficient.

Contributors

Wen-hao ZHANG wrote the first draft of this manuscript. Wen-hao ZHANG and Feng DING finished the numerical simulation. Jun LIU and Feng DING helped to organize the manuscript. Feng DING and Wei HUANG revised and edited the final version.

Conflict of interest

Wen-hao ZHANG, Jun LIU, Feng DING, and Wei HUANG declare that they have no conflict of interest.

References

ANSYS Inc., 2010. Ansys Fluent 13.0 Theory Guide. ANSYS Inc., Canonsburg, USA.

Barkmeyer DEF, Starkey RP, Lewis MJ, 2005. Inverse waverider design for inward turning inlets. Proceedings of the 41st AIAA/ASME/SAE/ASEE Joint Propulsion Conference & Exhibit. https://doi.org/10.2514/6.2005-3915

Billig FS, Kothari AP, 2000. Streamline tracing: technique for designing hypersonic vehicles. *Journal of Propulsion and Power*, 16(3):465-471. https://doi.org/10.2514/2.5591

Ding F, Liu J, Shen CB, et al., 2015. Novel inlet-airframe integration methodology for hypersonic waverider vehicles. *Acta Astronautica*, 111:178-197. https://doi.org/10.1016/j.actaastro.2015.02.016

Ding F, Liu J, Shen CB, et al., 2018. An overview of waverider design concept in airframe/inlet integration methodology for air-breathing hypersonic vehicles. *Acta Astronautica*, 152(1):639-656. https://doi.org/10.1016/j.actaastro.2018.09.002

Ferguson F, Dasque N, Mrema HF, et al., 2015. A coupled aerodynamic and propulsive performance analysis of the generic hypersonic vehicle. Proceedings of the 51st AIAA/SAE/ASEE Joint Propulsion Conference. https://doi.org/10.2514/6.2015-3839

Heiser WH, Pratt DT, 1994. Hypersonic Airbreathing Propulsion. AIAA, Washington, USA, p.24-26.

Kothari AP, Tarpley C, McLaughlin TA, et al., 1996. Hypersonic vehicle design using inward turning flow fields. Proceedings of the 32nd Joint Propulsion Conference and Exhibit. https://doi.org/10.2514/6.1996-2552

Li YQ, An P, Pan CJ, et al., 2014. Integration methodology for waverider-derived hypersonic inlet and vehicle forebody. Proceedings of the 19th AIAA International Space Planes and Hypersonic Systems and Technologies Conference.

https://doi.org/10.2514/6.2014-3229

Li YQ, Shi CG, Zhu CX, et al., 2018. Aerodynamic combination design concept for hypersonic waverider forebody and inward turning inlet. *Journal of Propulsion Technology*, 39(10):2320-2328 (in Chinese). https://doi.org/10.13675/j.cnki.tjjs.2018.10.016

Liao L, Yan L, Huang W, 2018. Mode transition process in a typical strut-based scramjet combustor based on a parametric study. *Journal of Zhejiang University-SCIENCE A (Applied Physics & Engineering)*, 19(6):431-451. https://doi.org/10.1631/jzus.A1700617

Qiao WY, Yu AY, Yang DW, 2018. Integration design of inward-turning inlets based on forebody shock wave. *Acta Aeronautica et Astronautica Sinica*, 39(10):60-71 (in Chinese).

Tian C, Li N, Gong GH, et al., 2013. A parameterized geometry design method for inward turning inlet compatible waverider. *Chinese Journal of Aeronautics*, 26(5):1135-1146. https://doi.org/10.1016/j.cja.2013.07.003

Walker S, Tang M, Morris S, et al., 2008. Falcon HTV-3X–a reusable hypersonic test bed. Proceedings of the 15th AIAA International Space Planes and Hypersonic Systems and Technologies Conference. https://doi.org/10.2514/6.2008-2544

Walker SH, Rodgers F, 2005. Falcon hypersonic technology overview. Proceedings of the AIAA/CIRA 13th International Space Planes and Hypersonics Systems and Technologies Conference. https://doi.org/10.2514/6.2005-3253

Wang CP, Tian X, Yang LF, et al., 2015. Preliminary integrated design of hypersonic vehicle configurations including inward-turning inlets. *Journal of Aerospace Engineering*, 28(6):04014143. https://doi.org/10.1061/(asce)AS.1943-5525.0000480

Wang JF, Cai JS, Liu CZ, et al., 2017a. Aerodynamic configuration integration design of hypersonic cruise aircraft with inward-turning inlets. *Chinese Journal of Aeronautics*, 30(4):1349-1362. https://doi.org/10.1016/j.cja.2017.05.002

Wang JF, Cai JS, Duan YH, et al., 2017b. Design of shape morphing hypersonic inward-turning inlet using multi-stage optimization. *Aerospace Science and Technology*, 66:44-58. https://doi.org/10.1016/j.ast.2017.02.018

Wang WX, Gu Q, Guo RW, 2017. Study of flow control of inward turning inlet. *Journal of Propulsion Technology*, 38(5):961-967 (in Chinese). https://doi.org/10.13675/j.cnki.tjjs.2017.05.001

Wang XD, Wang JF, Lyu ZJ, 2016. A new integration method based on the coupling of multistage osculating cones waverider and Busemann inlet for hypersonic airbreathing vehicles. *Acta Astronautica*, 126:424-438. https://doi.org/10.1016/j.actaastro.2016.06.022

Yang DW, Yu AY, Han YY, et al., 2019. Study on self-starting characteristics of an inward turning inlet. *Journal of Propulsion Technology*, 40(1):76-83 (in Chinese). https://doi.org/10.13675/j.cnki.tjjs.170782

Zhou H, Jin ZG, Zhang KY, 2018. Effects of entrance and exit aspect ratios on flow characteristics of inward turning inlets. *Journal of Propulsion Technology*, 39(12):2679-2684 (in Chinese). https://doi.org/10.13675/j.cnki.tjjs.2018.12.005

Zucrow MJ, Hoffman JD, 1977. Gas Dynamics, Vol. 2: Multidimensional Flow. John Wiley and Sons, Inc., New York, USA, p.112-294.

Zuo FY, Huang GP, Xia C, et al., 2015. Investigation of the self-starting ability of an internal waverider inlet for ramjet. Proceedings of the 51st AIAA/SAE/ASEE Joint Propulsion Conference. https://doi.org/10.2514/6.2015-3748

Zuo FY, Huang GP, Xia C, 2016. Investigation of internal-waverider-inlet flow pattern integrated with variable-geometry for TBCC. *Aerospace Science and Technology*, 59:69-77. https://doi.org/10.1016/j.ast.2016.10.009

中文概要

题　目： 新型内转式乘波前体-进气道一体化设计方法

目　的： 针对高超声速飞行过程中机体前缘和进气道之间相互影响的问题，本文从头部进气的角度出发，利用内转式进气道高总压恢复系数和高压缩效率的特性，探索前体与进气道的一体化设计。

创新点： 1. 提出一种内转式轴对称基准流场的构建方法，并设计生成内转式进气道；2. 设计内转式乘波前体/进气道一体化构型，并提出将进气道进口型线划分为前体前缘型线（FCC）和进气道唇口型线（LCC）。

方　法： 1. 构建内转式轴对称基准流场（图 9）；2. 在基准流场中生成内转式进气道并设计构造进气道外表面（图 13）；3. 通过仿真模拟，验证所提方法及原理的正确性和有效性（图 15~20）。

结　论： 1. 基于特征线理论，设计并求解内转式乘波前体/进气道轴对称基准流模型（IARFM），同时设计并生成了内转式进气道和外壁面；提出将进气道进口型线划分为前体前缘型线（FCC）和进气道唇口型线（LCC）。2. 提出了内转式乘波前体/进气道（ITWF）的一体化设计方法，并通过对无粘数值模拟结果与理论设计值的比较，验证了设计方法的正确性和有效性。3. 经过分析可知，激波形状和位置的数值模拟结果与基准流模型吻合较好。这些结果验证了无粘流设计条件下的一体化设计过程的正确性，且该一体化结构具有较高的总压恢复系数和气流捕获效率。

关键词： 高超声速；内转式乘波前体/进气道；轴对称基准流场模型；流线追踪